Dalton Transactions

ROYAL SOCIETY OF CHEMISTRY

PAPER

View Article Online
View Journal | View Issue

Cite this: *Dalton Trans.*, 2022, **51**, 4435

Synthesis–structure relationships in Li- and Mn-rich layered oxides: phase evolution, superstructure ordering and stacking faults†

Ashok S. Menon, ‡ Said Khalil, Dickson O. Ojwang, Kristina Edström, Cesar Pay Gomez and William R. Brant *

Li- and Mn-rich layered oxides are promising positive electrode materials for future Li-ion batteries. The presence of crystallographic features such as cation-mixing and stacking faults in these compounds make them highly susceptible to synthesis-induced structural changes. Consequently, significant variations exist in the reported structure of these compounds that complicate the understanding of how the crystallographic structure influences its properties. This work investigates the synthesis–structure relations for three widely investigated Li- and Mn-rich layered oxides: Li_2MnO_3, $Li_{1.2}Mn_{0.6}Ni_{0.2}O_2$ and $Li_{1.2}Mn_{0.54}Ni_{0.13}Co_{0.13}O_2$. For each compound, the average structure is compared between two synthetic routes of differing degrees of precursor mixing and four annealing protocols. Furthermore, thermodynamic and synthesis-specific kinetic factors governing the equilibrium crystallography of each composition are considered. It was found that the structures of these compounds are thermodynamically metastable under the synthesis conditions employed. In addition to a driving force to reduce stacking faults in the structure, these compositions also exhibited a tendency to undergo structural transformations to more stable phases under more intense annealing conditions. Increasing the compositional complexity introduced a kinetic barrier to structural ordering, making $Li_{1.2}Mn_{0.6}Ni_{0.2}O_2$ and $Li_{1.2}Mn_{0.54}Ni_{0.13}Co_{0.13}O_2$ generally more faulted relative to Li_2MnO_3. Additionally, domains with different degrees of faulting were found to co-exist in the compounds. This study offers insight into the highly synthesis-dependent subtle structural complexities present in these compounds and complements the substantial efforts that have been undertaken to understand and optimise its electrochemical properties.

Received 12th January 2022,
Accepted 15th February 2022

DOI: 10.1039/d2dt00104g

rsc.li/dalton

Introduction

Li- and Mn-rich layered oxides such as Li_2MnO_3, $Li_{1.2}Mn_{0.6}Ni_{0.2}O_2$ and $Li_{1.2}Mn_{0.54}Ni_{0.13}Co_{0.13}O_2$, are intensely investigated as positive electrode materials for future Li-ion batteries due to their high specific capacity, environmental benignity and low-cost.[1–3] The latter two compounds have been subject to a variety of efforts aimed at optimising their electrochemical performance as a step towards commercialization.[4–7] Despite the research attention, the crystallographic description of these materials suffers from a distinct lack of consensus,[8–10] possibly due to a high susceptibility to synthetic variations.[11–15] Previously, the interdependencies between the synthesis, composition and structure of (non-Li-rich) Li transition metal (TM) oxides have been explored through combinatorial studies.[16,17] Mapping out the phase diagram of these compositions have revealed their complexity where, up to three different crystallographic phases co-exist in certain regions of the thermodynamic phase space.[16,18] Synthetic parameters like annealing procedures and cooling rates have also been reported to influence the crystal structure of these systems.[12,19] Within this composition space, are the Li- and Mn-rich layered oxides. While many of the same trends observed for non-Li-rich compounds apply to these compounds, the synthesis-induced structural variations are amplified due to the presence of structural features like cation site-mixing and stacking faults, which are not typically found in the non-Li-rich systems.[20]

To understand the different ways synthesis can affect the structure of Li- and Mn-rich layered oxides, it is instructive to revisit their crystallography. Unlike non-Li-rich systems, Li- and Mn-rich layered oxides contain both Li and TMs in the

Department of Chemistry-Ångström Laboratory, Uppsala University, Box 538, SE-75121 Uppsala, Sweden. E-mail: william.brant@kemi.uu.se

† Electronic supplementary information (ESI) available: Structure models used to simulate XRD patterns, single peak-fitting, XRD data, ICP-OES results, Pawley refinements and structure analysis using FAULTS. Raw data and refinement files. See DOI: 10.1039/d2dt00104g

‡ Current address: Ashok S. Menon, WMG, University of Warwick, Coventry CV4 7AL, UK.

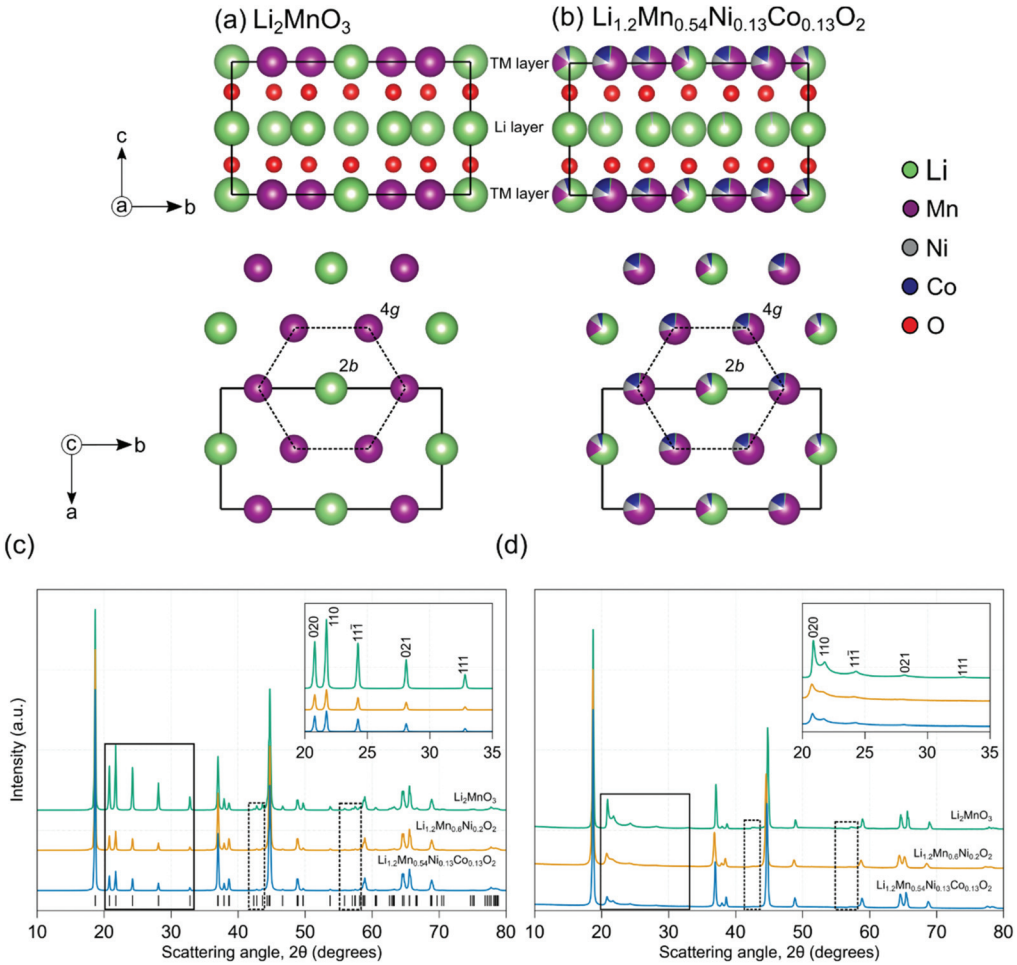

Fig. 1 Crystal structures of (a) Li_2MnO_3 and (b) $Li_{1.2}Mn_{0.54}Ni_{0.13}Co_{0.13}O_2$. Corresponding top-view of the TM-layers with the Wyckoff positions and hexagonal ordering highlighted, are shown below. Stack plots of simulated (c) and experimental (d) X-ray diffraction patterns (Cu-Kα) of Li_2MnO_3, $Li_{1.2}Mn_{0.6}Ni_{0.2}O_2$ and $Li_{1.2}Mn_{0.54}Ni_{0.13}Co_{0.13}O_2$. The superstructure reflections arising from cation ordering between 20° and 35° are highlighted in the inset as well as with solid rectangles, and indexed in the *C*2/*m* space group symmetry. Other superstructure reflections are highlighted using dashed boxes. In (c), simulated Bragg reflections were artificially broadened, to facilitate comparison with the experimental XRD pattern. The positions of the allowed Bragg reflections are shown using black ticks. Details of the structure models used to simulate the XRD patterns are provided in section 1 of the ESI.†

TM-layers (Fig. 1a and b). Due to size and Coulombic considerations, the Li- and TM-ions in this layer order hexagonally through the preferential occupation of the 2*b* (0, $\frac{1}{2}$, 0) and 4*g* (0, *y*, 0) Wyckoff positions (in the *C*2/*m* space group symmetry), respectively. This forms a superstructure on the parent rhombohedral cell, reducing the overall symmetry to monoclinic (Fig. 1a and b).[20] The superstructure ordering manifests in a diffraction pattern as superstructure reflections (Fig. 1c and d insets). In Li- and Mn-rich layered oxides, cation site-mixing occurs as a result of Li- and TM-ions mixing between the two sites within the TM-layers. This redistribution of Li and TM ions affects the intensity of superstructure reflections, which is determined by the difference in the average electronic density on the two cation sites in this layer.[11,21] Greater differences in the electronic density leads to greater X-ray scattering contrast between the two sites, which leads to more intense superstructure reflections. Among Li_2MnO_3, $Li_{1.2}Mn_{0.6}Ni_{0.2}O_2$ and $Li_{1.2}Mn_{0.54}Ni_{0.13}Co_{0.13}O_2$, the former has the most intense superstructure reflections as it has the highest average electronic density difference between the 2*b* and 4*g* sites, which are completely occupied by Li^+ and Mn^{4+}, respectively. The intensity of these reflections reduces in $Li_{1.2}Mn_{0.6}Ni_{0.2}O_2$ as Ni^{2+} occupies both sites leading to a decrease in the average difference between the electronic densities. Even in $Li_{1.2}Mn_{0.54}Ni_{0.13}Co_{0.13}O_2$ where all four cations may be found on each site,[22] superstructure reflections are still seen as the 2b position is preferentially occupied by the less-positively charged species (Li^+ and Ni^{2+}) and the 4g position, by the highly-charged Co^{3+} and Mn^{4+}. As illustrated by the differences in these reflections between the (defect-free) simulated (Fig. 1c) and experimental (Fig. 1d) diffraction patterns, cation ordering within the structures rarely conforms to ideality. The disruption of periodicity in the TM-layer cation ordering along the stacking direction (*c*) leads to stacking faults.[20]

Additionally, Ni^{2+} may migrate to the Li-layer and *vice versa*, resulting in Li–Ni interlayer mixing as reported in $Li_{1.2}Mn_{0.6}Ni_{0.2}O_2$ and $Li_{1.2}Mn_{0.54}Ni_{0.13}Co_{0.13}O_2$.[22,23]

Synthetic variations have been reported to create pronounced structural differences at the local and long-range length scales in Li- and Mn-rich layered oxides.[11,13–15,24–26] For $Li_{1.2}Mn_{0.54}Ni_{0.13}Co_{0.13}O_2$, the amount of trapped molecular O_2 in the bulk, resulting from O-redox at high voltages is also affected by synthesis method.[27] Motivated by these previous studies, the current work investigates the effect of two different synthesis methods and the associated annealing parameters for Li_2MnO_3, $Li_{1.2}Mn_{0.6}Ni_{0.2}O_2$ and $Li_{1.2}Mn_{0.54}Ni_{0.13}Co_{0.13}O_2$. Each compound was synthesised through two commonly used synthesis methods: citrate sol–gel and solid-state methods for Li_2MnO_3, and the citrate sol–gel and coprecipitation methods for the latter two.[28,29] The methods were chosen due to the differences in the nature and degree of mixing of the Li and TM precursors, which is expected to influence the cation ordering, and consequently, the degree of faulting in the as-synthesised samples. In the citrate sol–gel method, the crystallisation of the final product occurs from a 'single' metal-citrate complex precursor. In the solid-state (for Li_2MnO_3) and coprecipitation (for $Li_{1.2}Mn_{0.6}Ni_{0.2}O_2$ and $Li_{1.2}Mn_{0.54}Ni_{0.13}Co_{0.13}O_2$) methods, the crystallisation happens from a mix containing separate Li and TM precursors. Here, the solid-state and coprecipitation methods are functionally equivalent in terms of the degree of mixing of the Li and TM precursors. The nature and degree of precursor-mixing are also expected to influence the kinetic factors determining the synthesis progression, and consequently, the morphology and structure of the final product. Four different annealing procedures were chosen so that the effect of both the annealing temperature and duration could also be investigated. Comparing different annealing temperatures and durations provides information about the thermodynamic stability of the crystal structure as a function of temperature as well as the kinetics of the synthesis process. By investigating the structure of the samples produced *via* these methods with X-ray diffraction, the synthesis-induced bulk structural changes can be studied.

Experimental methods

Synthesis

The sol–gel samples were synthesised through a modified Pechini citrate sol–gel method.[30] For a typical synthesis, stoichiometric amounts of lithium acetate dihydrate ($CH_3COOLi{\cdot}2H_2O$, Sigma-Aldrich, reagent grade), manganese(II) acetate tetrahydrate ($(CH_3COO)_2Mn{\cdot}4H_2O$, Sigma-Aldrich, ≥99%), nickel(II) acetate tetrahydrate ($(CH_3COO)_2Ni{\cdot}4H_2O$, Sigma-Aldrich, ≥99%) and cobalt(II) acetate tetrahydrate ($(CH_3COO)_2Co{\cdot}4H_2O$, Sigma-Aldrich, ≥99%) were dissolved in 300 ml of deionized water. A 2.5 mol% excess of the Li source was added to compensate for the loss of Li during high-temperature annealing. A 300 ml aqueous solution of citric acid (Sigma-Aldrich, ≥99.5%) and EDTA (ethylenediaminetetraacetic acid, ACS reagent) was then prepared, and mixed with the previous solution. The cation-citric acid-EDTA molar ratio was approximately equal to 1 : 1.5 : 1. The two solutions were thoroughly mixed by magnetic stirring for ~1 h after which, the pH of the solution was adjusted to ~7.5 using ammonium hydroxide solution (NH_4OH, Sigma-Aldrich, 28–30%). The solution was heated at 120–150 °C overnight to form a dry gel that was then crushed into a powder. The powder was transferred to an alumina crucible and annealed in a muffle furnace in air at 550 °C (6 °C min^{-1} ramp) for 5 h, and then cooled down to room temperature in the furnace.

Precursors for the solid-state synthesis of Li_2MnO_3, were prepared by mixing stoichiometric amounts of Li_2CO_3 and MnO_2 using mortar and pestle. Like the sol–gel synthesis, 2.5 mol% excess of the Li source was used to account for the loss of Li during annealing. No pre-heating was performed for the solid-state synthesis.

For the coprecipitation synthesis of $Li_{1.2}Mn_{0.6}Ni_{0.2}O_2$ and $Li_{1.2}Mn_{0.54}Ni_{0.13}Co_{0.13}O_2$, precursors were prepared by thoroughly mixing stoichiometric amounts of Li_2CO_3 (with 2.5 mol% excess) and the corresponding mixed-TM hydroxide salts, *i.e.*, $[Mn_{0.75}Ni_{0.25}](OH)_2$ for $Li_{1.2}Mn_{0.6}Ni_{0.2}O_2$ and $[Mn_{0.675}Ni_{0.1625}Co_{0.1625}](OH)_2$ for $Li_{1.2}Mn_{0.54}Ni_{0.13}Co_{0.13}O_2$. For the coprecipitation process, the transition metal acetate salts (same as the ones used for the sol–gel synthesis) were dissolved in ~50 ml of deionised water as per stoichiometry and gradually added (~1 h) to a 400 ml aqueous solution of lithium hydroxide (LiOH, Sigma-Aldrich, reagent grade, 98%) under stirring. The LiOH solution was of higher molarity than the TM salt solution to ensure complete precipitation of the TM hydroxides. The precipitates thus formed were filtered and thoroughly washed 2–3 times to remove residual Li salts. It was then dried in air at 180 °C for 12 h and mixed with the appropriate amount of Li_2CO_3 using a mortar and pestle. Samples were then heated at 550 °C for 5 h (6 °C min^{-1} ramp) in an alumina crucible using a muffle furnace in air to obtain the precursor for the final annealing.

The final annealing for all precursors (contained in alumina crucible) was carried out in air using four different protocols: (1) 900 °C – 3 h, (2) 950 °C – 3 h, (3) 1000 °C – 3 h and (4) 900 °C – 15 h. In each case, 6 °C min^{-1} heating rate was used. Finally, samples were quenched to room temperature by bringing the crucible in contact with an aluminium plate. A schematic illustration of the different synthesis processes is shown in Fig. 2.

Characterization

Elemental analyses were carried out by inductively coupled plasma optical emission spectroscopy (ICP–OES) measurements using a PerkinElmer ICP–OES Avio 200 system. In each case, 5 mg of the sample was dissolved in a HCl–HNO_3 (3 : 1 v/v) solution (ICP-grade) and diluted to the required concentration using a 5 vol% aqueous solution of HNO_3, prepared using ultra-pure Milli-Q water (blank). The PerkinElmer Pure Plus Multi-element calibration standard was used as the reference for the ICP–OES measurements. Irrespective of the com-

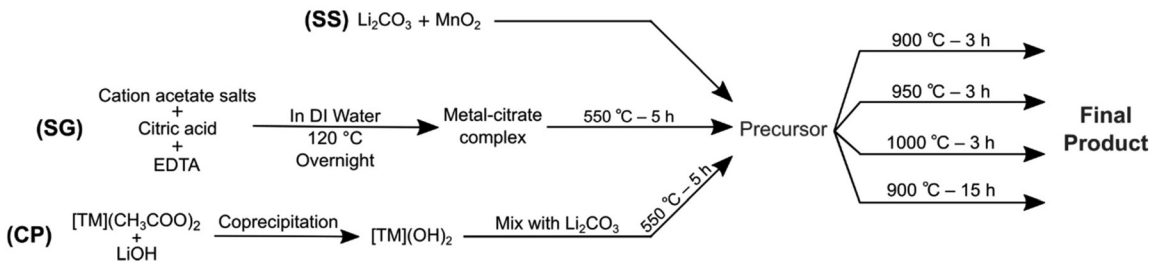

Fig. 2 Schematic illustration of the different synthesis routes. SS, SG and CP refer to solid-state, citrate sol–gel and coprecipitation methods, respectively.

position, Li, Mn, Ni, Co and Al concentrations were analysed to ensure that no cross-contamination had occurred.

Scanning electron microscopy (SEM) images were acquired using a Zeiss LEO 1530 scanning electron microscope. The samples were ground and spread on a carbon tape and coated with a thin layer of AuPd alloy to prevent charging. The images were obtained at an accelerating voltage of 1 kV by using the InLens detector.

X-ray powder diffraction data were collected on a Bruker D8 Advance Twin–Twin diffractometer (40 kV, 40 mA) using Cu-Kα radiation in Bragg–Brentano mode. The powdered samples were prepared for measurement by evenly spreading it out on zero-background Si sample holders. Data were collected using a Lynxeye XE-T position sensitive detector operated over an angular (2θ) range between 10–80° using a step size and time per step of 0.015° and 0.75 s, respectively. The sample holder was rotated (~15 rotations per min) for all measurements. The instrumental parameters and emission profile of the diffractometer were determined using the NIST 660c LaB_6 standard reference material. A small amount of tungsten Lα radiation was observed in the diffraction data.

A qualitative comparison of the cation site-mixing and stacking faults were performed using the amplitude (peak height) of the 020 reflection normalized to the 001 reflection and the peak broadening of the superstructure reflections, respectively.[11] The normalized amplitude of the 020 reflection is inversely proportional to the degree of cation site-mixing. Additionally, cation site-mixing does not affect the profile of the superstructure reflections, unlike stacking faults which imparts a strong asymmetry, especially to the 020 reflection.[31,32]

Simulation of the XRD patterns (Fig. 1c), Pawley refinements[33] of the unit cells and single peak fitting (for domain size calculations) were carried out using the TOPAS-Academic (v6) software.[34] Refinement of structure models with stacking faults, adapted from Serrano-Sevillano *et al.*,[13] were carried out using FAULTS software.[35]

Results & discussion

Li_2MnO_3, $Li_{1.2}Mn_{0.6}Ni_{0.2}O_2$ and $Li_{1.2}Mn_{0.54}Ni_{0.13}Co_{0.13}O_2$ are henceforth shortened to LMO, LMNO and LMNCO, respectively. The synthesis methods are denoted as SG (sol–gel), SS (solid-state) and CP (coprecipitation). Annealing procedures are also shortened appropriately. For example, 900C-3h represents an annealing temperature and duration of 900 °C and 3 h, respectively. The different samples (24 in total) belonging to the three compositions, each synthesised through two methods and four annealing procedures are tabulated in Table 1.

Morphology & crystallographic domain sizes

Morphological investigations were performed through scanning electron microscopy (SEM) imaging of the samples annealed using the 900C-3h procedure. Only this set was investigated as the effects of increased annealing conditions, at the microscopic level, are expected to primarily affect the particle sizes.[15,24] The SEM images shown in Fig. 3a, demonstrate that the samples predominantly differ in terms of the degree of agglomeration and consequently, the particle surface area. SG-LMO is composed of loosely bound crystallites that do not agglomerate, resulting in substantial free space between them. Contrarily, SS-LMO has larger crystallites that form tightly packed μm-sized agglomerations. In either case, the crystallites do not possess any specific shape, a trait common to all samples. SG-LMNO and SG-LMNCO are comparable to SG-LMO and are composed of similarly sized individual crystallites that do not agglomerate to any appreciable degree. On the other hand, the crystallites of CP-LMNO and CP-LMNCO agglomerate to form secondary particles a few μm in size; smaller than that seen in SS-LMO. Thus, the primary difference between the samples is that, irrespective of the composition, the SG-samples forms loosely bound individual crystallites with higher particle surface area as compared to their

Table 1 The compositions, synthesis methods and annealing procedures investigated in this work

Composition	Synthesis method	Annealing procedures
Li_2MnO_3 (LMO)	Sol–gel (SG)	
	Solid-state (SS)	900 °C – 3 h
$Li_{1.2}Mn_{0.6}Ni_{0.2}O_2$ (LMNO)	Sol–gel (SG)	950 °C – 3 h
	Coprecipitation (CP)	1000 °C – 3 h
$Li_{1.2}Mn_{0.54}Ni_{0.13}Co_{0.13}O_2$ (LMNCO)	Sol–gel (SG)	900 °C – 15 h
	Coprecipitation (CP)	

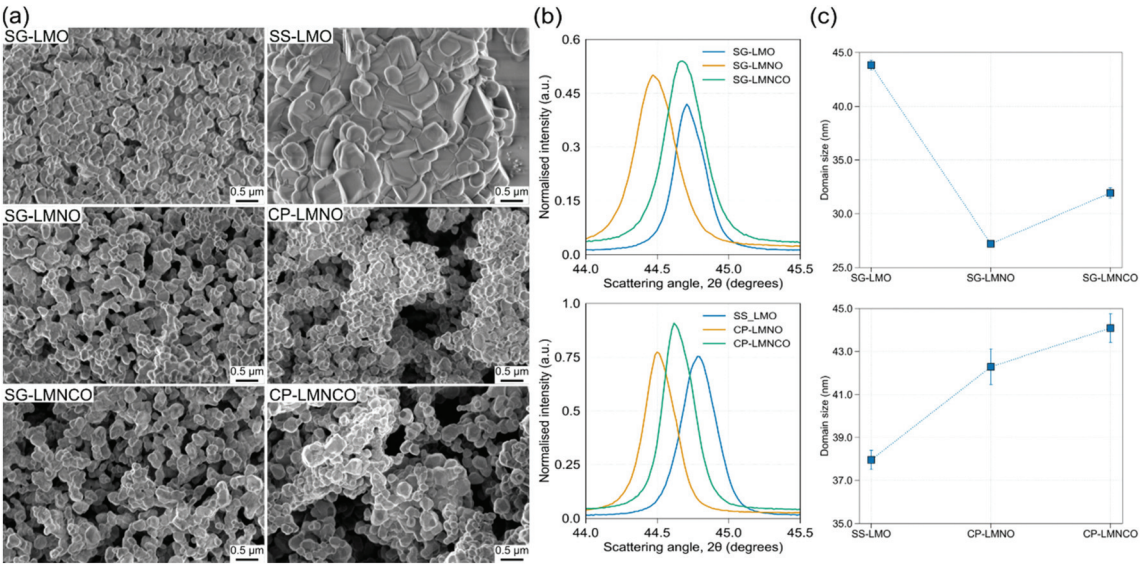

Fig. 3 (a) SEM images of the six samples annealed at 900 °C for 3 h. The sample name and scale bar are shown at the top-left and bottom-right, respectively. (b) The XRD peak at ~44.5° (Cu-Kα) used for the single-peak fitting. (c) Domain sizes calculated from the single-peak fitting.

corresponding SS- and CP-counterparts, which form μm-sized agglomerations. Comparable results were reported for similar materials and synthesis methods previously.[11,27,36]

The coherently diffracting domain size of the same samples (not to be confused with particle size), which provides insight into the size of ordered structural domains, was calculated by fitting the X-ray diffraction (XRD) peak at 44.5° (Fig. 3b), the details of which are provided in section 2 of the ESI.† It is worth noting that regions with varying amounts of stacking faults in the bulk complicates the definition of an 'ordered' domain, making the interpretation of absolute domain size values difficult. Also note that the peak at 44.5° is composed of three Bragg reflections (220, 20$\bar{2}$, 131). Nevertheless, the fitting can facilitate a qualitative comparison of the domain sizes in the samples. As shown in Fig. 3c, among the SG samples, LMNO and LMNCO have smaller domain sizes than LMO. However, the reverse is observed in samples prepared *via* SS and CP, with CP-LMNO and CP-LMNCO exhibiting larger domain sizes than SS-LMO. For the SG-synthesised samples, the decrease in the (ordered) domain sizes upon the cationic substitution of LMO could be due to the disruption of periodicity by the additional cations (Ni, Co). In other words, the TM-substitutions offer additional degrees of freedom to structural ordering, which hinders long-range structural periodicity. In the CP- and SS-samples, the difference in the domain size trends may be due to two factors. As will be discussed in a later section, these samples show evidence for the presence of regions with different degrees of faulting within the structure. Additionally, dissimilarities in the TM precursor salts (TM-hydroxides for LMNO and LMNCO, and MnO_2 for LMO) could also play a role in determining the degree of order in the structure due to the differences in their thermal degradation pathways. Nonetheless, both the composition and synthesis route, particularly the nature and degree of precursor-mixing, affect the crystallographic ordering and morphology of Li- and Mn-rich layered oxides.

Bulk structural changes

X-ray diffraction (XRD) data of all the samples is shown in Fig. 4. Expectedly, the samples share structural similarities and show comparable trends in their response to synthetic changes. Notably, higher annealing temperatures lower the asymmetry of the superstructure reflections (insets) signifying the reduction of stacking faults and growth of cationic ordering. This indicates the existence of a thermodynamic driving force for the reduction of faulting in the structure, irrespective of the composition. Increasing annealing duration (900C-15h) also reduces faulting and increases cation ordering, revealing the influence of kinetic factors on structural ordering. Additionally, increasing annealing temperature and duration lead to the growth of spinel and rock salt phases in most samples.[16–18] Taken together, these results suggest that pure phases of the layered structures with the three compositions investigated are thermodynamically metastable when synthesized using these routes and annealing conditions, all of which are commonly utilised in literature. Although the synthesis-induced changes in the structure are qualitatively similar, the degree to which they occur varies inconsistently, and therefore warrants closer inspection.

LMO

A magnified view of the XRD data, focusing on specific angular regions are shown in Fig. 5. Both the SG- and SS-samples synthesised at 900C-3h possess strongly asymmetric superstructure reflections, indicating the presence of stacking faults in the structure. However, the superstructure reflections

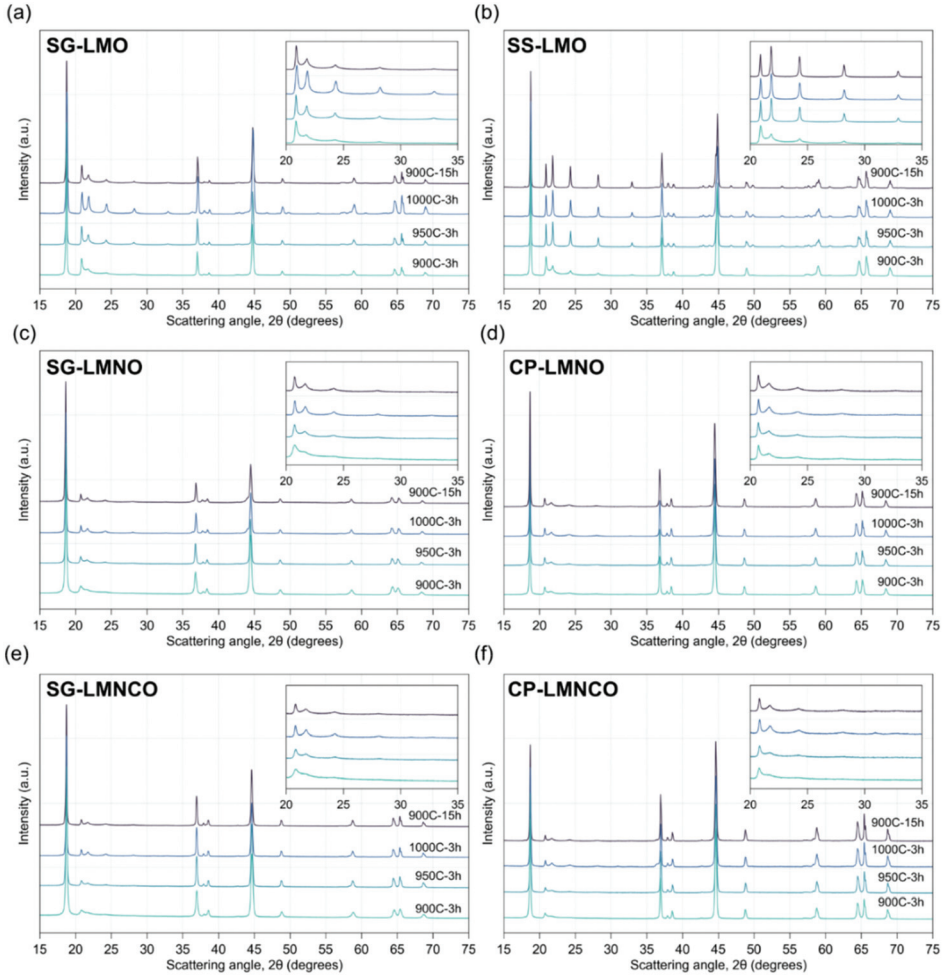

Fig. 4 Stacked XRD (Cu-Kα) patterns of the different samples, offset along *y* (a–f). The superstructure reflections in the 20–35° angular range are highlighted in the inset. The sample name is shown in the top-left corner and the annealing conditions, on the bottom right. Intensities have been normalized to the largest value in the corresponding measurement to aid comparison.

of the SS-sample are more intense, and the normalised amplitudes of these reflections are also higher for the SS-sample, indicating that the SS-sample has a higher degree of Li–Mn ordering within the TM-layer as well as along the stacking direction after the 900C-3h annealing. Increasing the annealing temperature from 900 to 950 °C leads to a marked deviation in the structural response of the samples. In the SS-sample, the amplitude of the 110 reflection (see Fig. 1c) becomes higher than that of 020 with a near-complete loss in the reflection asymmetry. In contrast, the SG-sample still retains the strongly asymmetric superstructure reflections. This observation, in addition to evidencing the higher cation ordering in SS-LMO, illustrates the ability of that sample to achieve structural ordering faster than SG-LMO. The 1000C-3h annealing leads to more-intense less-asymmetric superstructure reflections in both samples, together with the formation of the spinel and rock salt phases (Fig. 5 right panels). SG-LMO shows a comparatively higher amount of the new phases, as seen from the stronger spinel and rock salt peaks in Fig. 5a (right). This is also evidenced by the broadening of the 001 reflection, which is now composed of multiple reflections as shown in the ESI (Fig. S1a of ESI†). No such feature is observed for SS-LMO (Fig. S1b†), where the spinel and rock salt phases are formed to a much lower extent. Interestingly, even after the 1000C-3h annealing, SG-LMO remains faulted, unlike SS-LMO. Increasing the annealing duration from 3 to 15 h (at 900 °C) also elicits substantially different responses from the samples. In SG-LMO, the superstructure reflections are comparable to those seen for 950C-3h treatment. Contrarily in SS-LMO, the longer annealing leads to symmetric superstructure reflections of higher intensity and sharper than in the 1000C-3h sample. Furthermore, a peak corresponding to a rock salt phase[18] is found in SG-LMO when annealed at 900 °C (for both 3 and 15 h) which is absent in SS-LMO. Based on these results, it is certain that stacking faults in SG-LMO cannot be eradicated by increasing the annealing temperature as the layered structure decomposes to spinel and rock salt phases. Increasing the annealing duration is another option

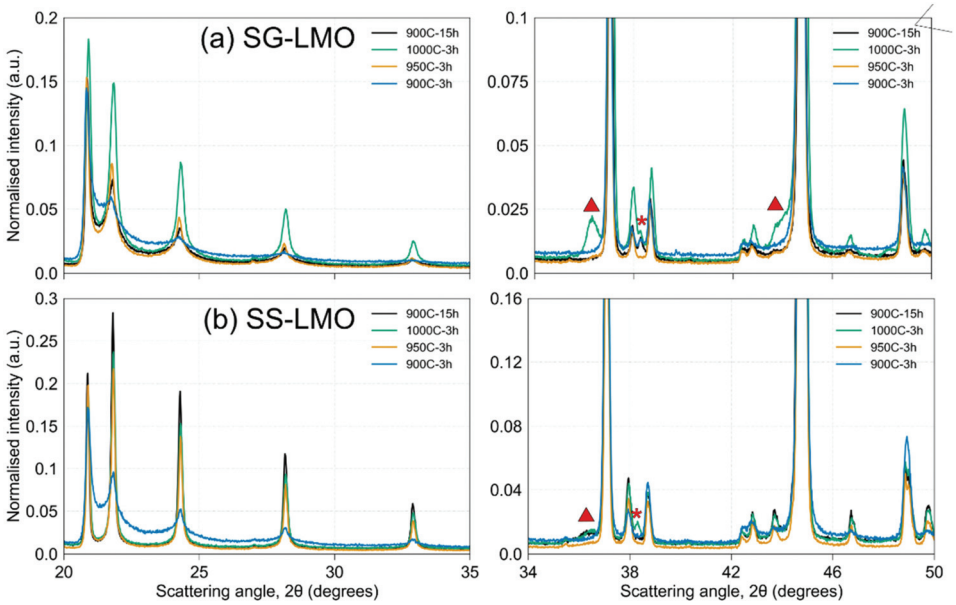

Fig. 5 Magnified view of the XRD (Cu-Kα) data of (a) SG- and (b) SS-LMO. Spinel and rock salt phases are highlighted using coloured triangles and asterisks, respectively. Intensities have been normalized to the largest value in the corresponding measurement to aid comparison.

but a complete eradication of faulting is unlikely within reasonable annealing times of 15–20 h. This accentuates the synthesis-dependent kinetics at play once again, wherein the growth of cation ordering is expedited in the solid-state-synthesised LMO samples. The key to rationalising these observations lie in the differences in the synthesis methods.

The thermodynamic and kinetic factors governing the response of the LMO samples to different annealing conditions is determined by the nature of precursors, their mixing, and the crystallisation mechanisms. The crystallisation of SG-LMO occurs from a metal-citrate matrix with the concomitant decomposition of organic matter as gaseous species. The evolution of gaseous species creates free space within the reaction matrix and leads to the formation of loosely bound crystallites, as seen in Fig. 3a.[11] On the other hand, SS-LMO is formed by the solid-state reaction between MnO_2 and Li_2CO_3, because of which tightly packed crystallite agglomerates are formed. Although O_2 and CO_2 gases are evolved during the SS-synthesis reaction, it is substantially lower than the gas evolved in the SG-synthesis.[11] Both these reasons, *i.e.*, the presence of organic matter during crystallisation and the loosely packed crystallites, leads to structural and morphological differences in the SG- and SS-LMO samples. Firstly, the presence of organic matter in the SG-LMO precursor can impede structural ordering and removal of faulting. Secondly, the increased free-space between the SG-crystallites hinders crystallite-growth and agglomeration and leads to a sample with higher surface area. Although not strongly observed in the ICP–OES data (section 4 of ESI†), the higher tendency of SG-LMO to undergo structural decomposition may be ascribed to the increased Li and O loss[27] through volatilisation facilitated by the high crystallite/sample surface area. This leads to a surface-to-bulk concentration gradient promoting the growth of spinel and rock salt phases.

LMNO

The structure of LMNO is derived from that of LMO by replacing a portion of Li and Mn in the TM layer by Ni. Based on the stoichiometry, the highest degree of cation ordering (for this composition) is achieved when 40% of the Li (2b) and 10% of the Mn (4g) sites are occupied by Ni, which is also chemically reasonable considering the similar ionic radius of Ni^{2+} and Li^{+}. The amplitude of the 020 reflection, a qualitative measure of the TM-layer cation ordering, does not change significantly with increasing annealing temperature and duration, unlike LMO. Contrarily, as there is reduction in the asymmetry of the superstructure peaks, increasing the annealing conditions does lead to a reduction in the degree of faulting. However, this reduction happens much slower when compared to LMO, evidencing that the driving force towards greater cation ordering along the stacking direction is much smaller in LMNO. The presence of the larger Ni^{2+} also hinders the growth of structural order. Previously, increased Ni content was reported to increase the degree of faulting in Li- and Mn-rich nickel oxides.[37] It is worth mentioning that higher annealing temperatures and durations are not able to completely eradicate stacking faults in the structure.

Like LMO, new peaks are observed in the SG-LMNO XRD data (Fig. 6) after the 1000C-3h and 900C-15h treatments. Considering the similarity of these peaks to that observed in LMO, they are inferred to belong to spinel and/or rock salt Li–TM–O phases. However, the amount of these phases formed are comparatively lower in LMNO, indicating that Ni substitution retards their growth. Furthermore, compared to the

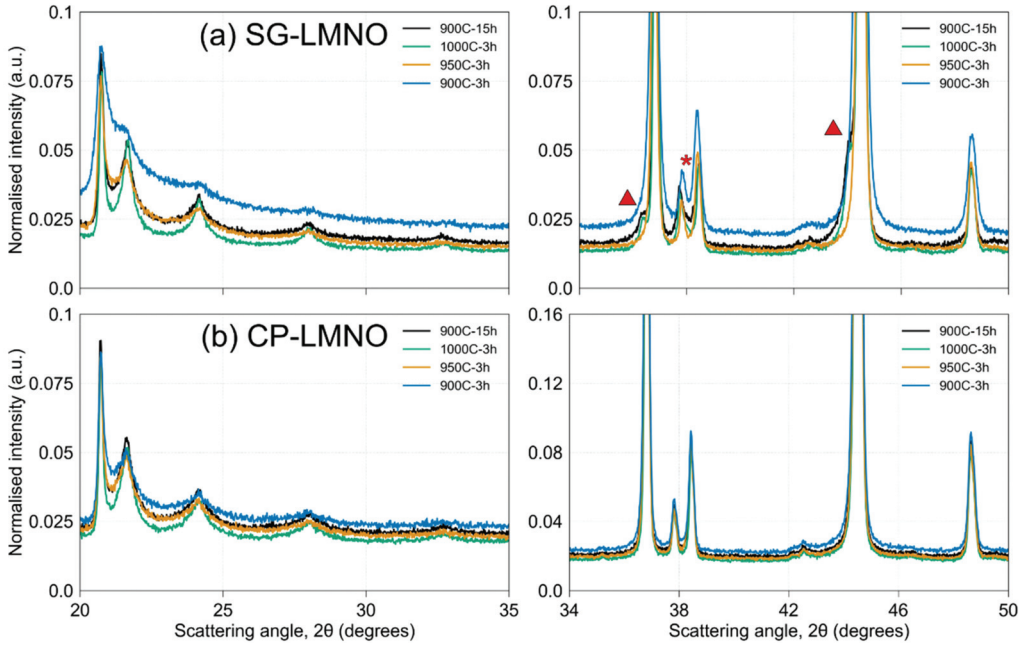

Fig. 6 Magnified view of the XRD (Cu-Kα) data of (a) SG- and (b) CP-LMNO. Spinel and rock salt phases are highlighted using coloured triangles and asterisks, respectively. Intensities have been normalized to the largest value in the corresponding measurement to aid comparison.

900C-15h annealing, the 1000C-3h procedure leads to more intense superstructure reflections, indicating that annealing temperature has a higher impact on the reduction of faulting than the annealing duration. This highlights the role of the larger Ni^{2+} in hindering the growth of structural order. Like in SG-LMO, the presence of organic components in SG-precursor and their increased surface area leads to the slower kinetics of stacking fault reduction and increased susceptibility to structural decomposition into spinel and rock salt phases, compared to CP-LMNO. The SG-samples with its higher surface area are susceptible to higher Li loss from the surface, thereby accelerating the decomposition of the layered structure. Intriguingly, none of the CP-LMNO samples showed any significant amount of these phases. While *in situ* studies are

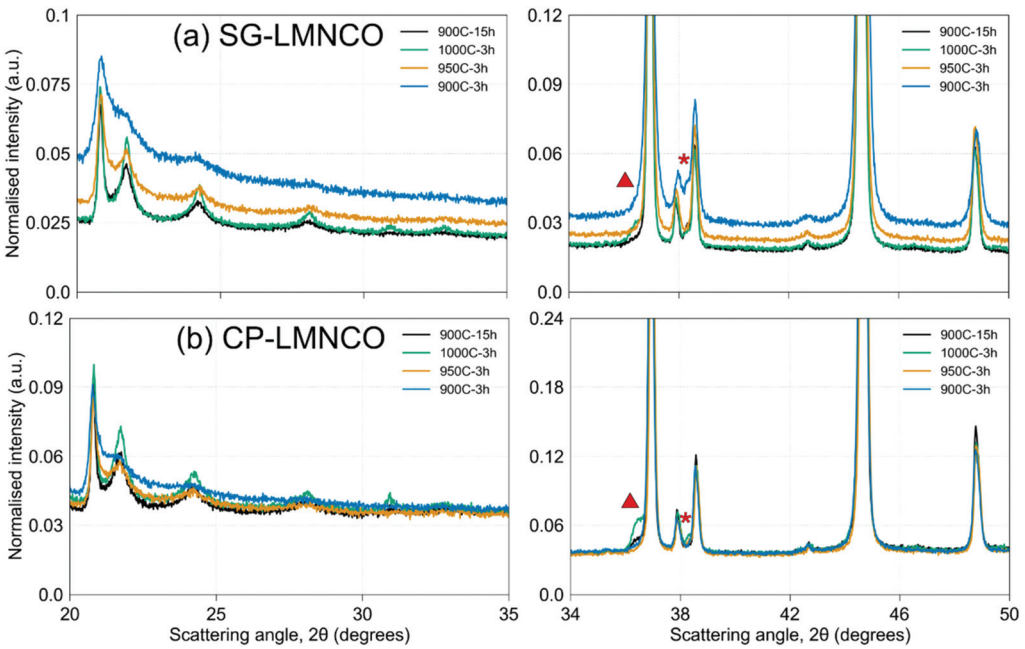

Fig. 7 Magnified view of the XRD (Cu-Kα) data of (a) SG- and (b) CP-LMNCO. Spinel and rock salt phases are highlighted using coloured triangles and asterisks, respectively. Intensities have been normalized to the largest value in the corresponding measurement to aid comparison.

necessary to understand the reason behind the behaviour of CP-samples, these results illustrate the strong influence of synthesis precursors on the structure of Li- and Mn-rich layered oxide phases, even when the targeted composition is the same.

LMNCO

Many of the LMNO sample trends are also found in LMNCO. As shown in Fig. 7, LMNCO samples exhibit the same progressive asymmetry loss of the superstructure reflections with increasing annealing temperature and duration, indicating the decrease of faulting in the structure. Additionally, like in LMNO, there is a high degree of TM-layer Li–TM ordering in the LMNCO samples, which does not significantly change with more severe annealing. Here, a high degree of ordering refers to the scenario where the average electronic density difference between the two TM-layer sites is maximum for the specific composition (Table S7 of ESI†). Stacking faults on the other hand, are found to decrease with higher annealing temperature and duration. The formation of new phases in LMNCO after the 1000C-3h and 900C-15h annealing is also different to that of LMNO. For example, the 1000C-3h SG-LMNCO sample has a comparatively lower amount of the spinel phase as compared to SG-LMNO synthesised under the same conditions. Additionally, unlike CP-LMNO, CP-LMNCO shows pronounced formation of the spinel and rock salt phases. Thus, the introduction of Co into the structure significantly affects the temperature-dependent structural evolution. However, it must be noted that the intensity differences between the phases formed could also arise from the differences in elemental composition of the phases. This is illustrated in Fig. 7b (left panel) where a weak reflection is observed at ~31°, which is expected to belong to a spinel phase as per previous reports.[38] Note that this reflection is not present in the LMO or LMNO samples.

Unit-cell changes and structural refinements

Like the SEM investigation, only the 900C-3h samples were comparatively analysed using Pawley and structural refinements. This is because accurate structural and compositional

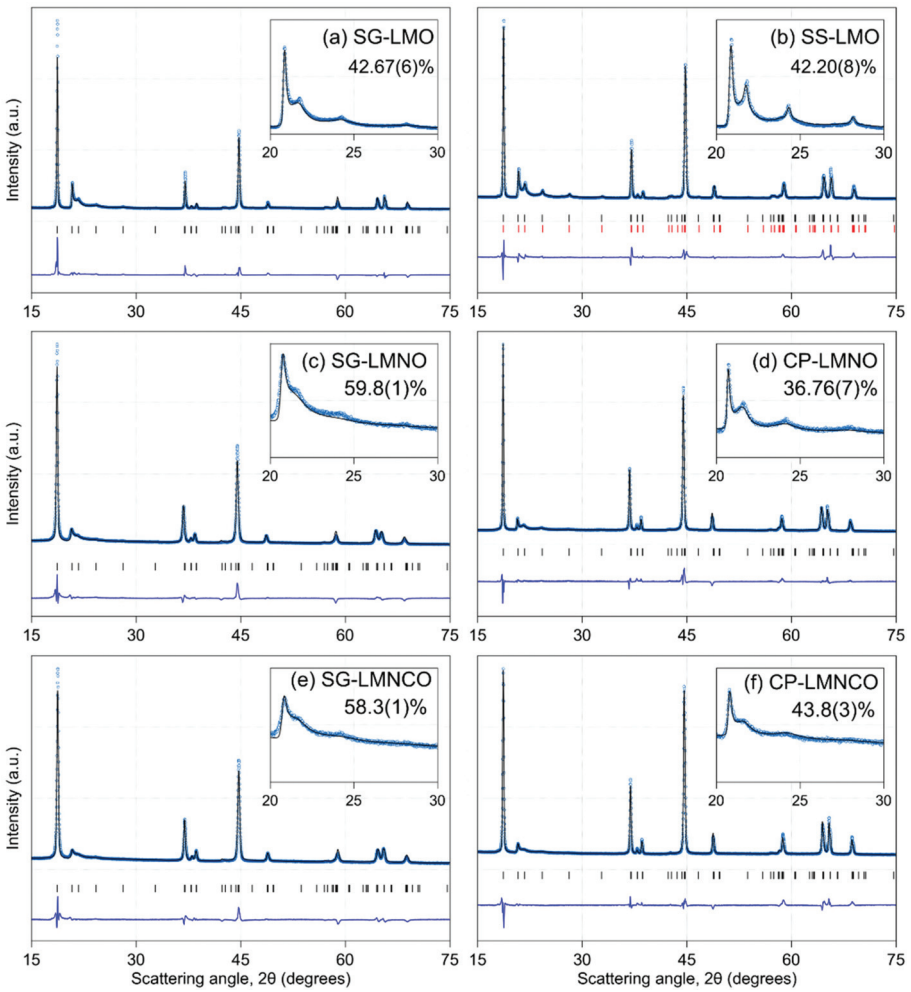

Fig. 8 FAULTS refinement plots of the different samples (a–f). The observed and calculated intensities are shown as blue circles and black lines, respectively. The difference curve is shown in navy blue and the positions of the Bragg reflections as vertical tick markers. In (b) the black and red markers denote faulted and fault-free Li_2MnO_3 phases, respectively.

characterisation of the layered, spinel and rock salt phases solely using laboratory XRD data is difficult due to severe peak overlap between the phases and the reduced X-ray scattering contrasts of the TMs. Pawley fitting of the XRD data was carried out with a $C2/m$ unit cell. The results are as expected with the inclusion of additional cations (Ni for LMNO, Ni and Co for LMNCO) leading to an expansion of the unit cell. Brief discussion of the results can be found in ESI section 5.† Structural refinement using FAULTS was carried out to quantitatively analyse the degree of faulting in the six samples. The refinement plots are shown in Fig. 8, and the refinement methodology and results are elaborated in the ESI (section 6†). Due to the low sensitivity of X-rays to Li and O, and the reduced X-ray scattering contrast between the TMs, the discussion has been limited to the results obtained from the fitting of the superstructure reflections between 20 and 35°. Apart from SS-LMO, where a satisfactory fit was obtained only using a combination of a faulted and fault-free LMO phase, all the other samples were fit using a structure model with a single degree of faulting. As shown in Fig. S3 (ESI†), using a single faulted LMO phase to fit SS-LMO, results in a visibly poor fit to the superstructure reflections. Similar results were also obtained in our previous work on LMO.[11] The joint existence of faulted and fault-free domains in SS-LMO might be the reason for its lower domain size compared to SG-LMO (Fig. 3c). The fits to the LMNO and LMNCO superstructure reflections (both SG and CP) although satisfactory, are not perfect, indicating that domains with different degrees of faulting might also be present in these samples. Furthermore, the degree of faulting is found to vary with synthesis method. The CP-LMNO and CP-LMNCO samples possess a lower degree of faulting (*i.e.*, higher cation ordering along the stacking direction) which also conforms to the domain sizes shown in Fig. 3c, where it is seen that the ordered domain sizes in the CP samples is larger than their SG counterparts. Also of note is that satisfactory fit to the superstructure reflections were obtained without refining the cation occupancies of the two TM-layer sites, which were set to the scenario with highest degree of Li–TM order for that composition (Table S10 and section S6 in ESI†). This suggests that there is a high degree of TM-layer cation ordering in all the samples and that choice of synthesis method does not play a significant role in it.

Conclusion

The synthesis–structure relationships in Li_2MnO_3, $Li_{1.2}Mn_{0.6}Ni_{0.2}O_2$ and $Li_{1.2}Mn_{0.54}Ni_{0.13}Co_{0.13}O_2$ were investigated as a function of precursor mixing and annealing conditions. The degree of precursor mixing was controlled based on the synthetic approach, by employing a citrate sol–gel method with a single metal-citrate precursor and, solid-state (for Li_2MnO_3) and coprecipitation (for $Li_{1.2}Mn_{0.6}Ni_{0.2}O_2$ and $Li_{1.2}Mn_{0.54}Ni_{0.13}Co_{0.13}O_2$) methods with two-component precursors. Comparative analyses of the samples showed that they were thermodynamically metastable under the synthesis conditions employed in this study. Irrespective of the composition, stacking faults were not favoured and the amount of stacking faults reduced upon extended annealing. This driving force to reduce faulting is lower in $Li_{1.2}Mn_{0.6}Ni_{0.2}O_2$ and $Li_{1.2}Mn_{0.54}Ni_{0.13}Co_{0.13}O_2$ compared to Li_2MnO_3 due to the increased degree of compositional freedom, which makes it difficult to attain an ordered energy minimum, like the Li–TM TM-layer hexagonal ordering found in Li_2MnO_3. Although high-temperature and long-term annealing was successful in reducing the structural faulting, growth of spinel and rock salt phases were also observed in most samples. The sol–gel samples were more prone to the growth of these phases, which may be attributed to their smaller, loosely packed, high surface area crystallites. The higher surface area facilitates increased Li loss leading to surface-to-bulk Li gradient that subsequently leads to structural rearrangement to more stable phases. The sol–gel samples also displayed increased resistance to growth of ordered domains and the reduction of faulting in the structures. This was hypothesised to stem from the presence of organic matter in the sol–gel precursor whose decomposition happens simultaneously with the crystallisation process, thereby hindering the formation of atomic ordering in the structure. Therefore, minimising the synthesis-dependent kinetic barriers is a possible way to produce a high-degree of crystallographic ordering these samples.

Taken together, these results highlight the influence of synthesis on the structure and morphology of the samples. A key point of note is that the observed results do not follow conventional wisdom. For LMNO and LMNCO, despite the more intimate cation mixing in the 'single' SG precursor, structural order is greater in the CP method with two separate Li and TM precursor components. The same behaviour is also seen for LMO, where the SS-sample crystallises with a higher degree of order than the SG-sample with a single precursor. The amplified effect of synthesis routes and conditions on the as-synthesised crystal structure may also be the root cause behind the single- *vs.* multi-phase structural debate plaguing these materials. It is hoped that this work precludes the assumption that a 'universal' structure model is valid for this material system and promotes more in-depth synthesis–structure studies. This study contributes to the current understanding of the synthesis–structure relationships in Li- and Mn-rich layered oxides and serves as a platform for further work in controlling the crystal structure of these compounds through synthetic pathways.

Conflicts of interest

The authors declare no competing financial interest.

Acknowledgements

Funding sources: This research is funded by the Swedish Foundation for Strategic Research (SSF) within the Swedish

National Graduate School in Neutron Scattering, SwedNess (GSn15 – 0008). The authors also gratefully acknowledge funding from the Strategic Research Area StandUp for Energy and the Swedish Energy Agency. The Swedish Research Council, VR, is also acknowledged (Grant No: 349-2014-3946). Said Khalil is grateful to the Swedish Institute for scholarship received for carrying out the project at Uppsala University.

References

1 M. M. Thackeray, S.-H. Kang, C. S. Johnson, J. T. Vaughey, R. Benedek and S. A. Hackney, Li_2MnO_3-stabilized $LiMO_2$ (M = Mn, Ni, Co) electrodes for lithium-ion batteries, *J. Mater. Chem.*, 2007, **17**(30), 3112–3125.

2 P. Rozier and J. M. Tarascon, Li-Rich Layered Oxide Cathodes for Next-Generation Li-Ion Batteries: Chances and Challenges, *J. Electrochem. Soc.*, 2015, **162**(14), A2490–A2499.

3 Z. Lu, D. D. MacNeil and J. R. Dahn, Layered Cathode Materials $Li[Ni_xLi_{(1/3-2x/3)}Mn_{(2/3-x/3)}]O_2$ for Lithium-Ion Batteries, *Electrochem. Solid-State Lett.*, 2001, **4**(11), A191.

4 D. Eum, B. Kim, S. J. Kim, H. Park, J. Wu, S. P. Cho, G. Yoon, M. H. Lee, S. K. Jung, W. Yang, W. M. Seong, K. Ku, O. Tamwattana, S. K. Park, I. Hwang and K. Kang, Voltage decay and redox asymmetry mitigation by reversible cation migration in lithium-rich layered oxide electrodes, *Nat. Mater.*, 2020, **19**(4), 419–427.

5 J. Lee, Y. Gong, L. Gu and B. Kang, Long-Term Cycle Stability Enabled by the Incorporation of Ni into Li2MnO3 Phase in the Mn-Based Li-Rich Layered Materials, *ACS Energy Lett.*, 2021, **6**(2), 789–798.

6 Z. Zhu, D. Yu, Y. Yang, C. Su, Y. Huang, Y. Dong, I. Waluyo, B. Wang, A. Hunt, X. Yao, J. Lee, W. Xue and J. Li, Gradient Li-rich oxide cathode particles immunized against oxygen release by a molten salt treatment, *Nat. Energy*, 2019, **4**(12), 1049–1058.

7 C. Cui, X. Fan, X. Zhou, J. Chen, Q. Wang, L. Ma, C. Yang, E. Hu, X. Q. Yang and C. Wang, Structure and Interface Design Enable Stable Li-Rich Cathode, *J. Am. Chem. Soc.*, 2020, **142**(19), 8918–8927.

8 H. Zheng, X. Han, W. Guo, L. Lin, Q. Xie, P. Liu, W. He, L. Wang and D.-L. Peng, Recent developments and challenges of Li-rich Mn-based cathode materials for high-energy lithium-ion batteries, *Mater. Today Energy*, 2020, 100518.

9 S. Hu, A. S. Pillai, G. Liang, W. K. Pang, H. Wang, Q. Li and Z. Guo, Li-Rich Layered Oxides and Their Practical Challenges: Recent Progress and Perspectives, *Electrochem. Energy Rev.*, 2019, **2**(2), 277–311.

10 N. Kireeva and V. S. Pervov, Materials Informatics Screening of Li–Rich Layered Oxide Cathode Materials with Enhanced Characteristics Using Synthesis Data, *Batteries Supercaps*, 2020, **3**(5), 427–438.

11 A. S. Menon, D. O. Ojwang, T. Willhammar, V. K. Peterson, K. Edstrom, C. P. Gomez and W. R. Brant, Influence of Synthesis Routes on the Crystallography, Morphology, and Electrochemistry of Li_2MnO_3, *ACS Appl. Mater. Interfaces*, 2020, **12**(5), 5939–5950.

12 T. Matsunaga, H. Komatsu, K. Shimoda, T. Minato, M. Yonemura, T. Kamiyama, S. Kobayashi, T. Kato, T. Hirayama, Y. Ikuhara, H. Arai, Y. Ukyo, Y. Uchimoto and Z. Ogumi, Dependence of Structural Defects in Li_2MnO_3 on Synthesis Temperature, *Chem. Mater.*, 2016, **28**(12), 4143–4150.

13 J. Serrano-Sevillano, M. Reynaud, A. Saracibar, T. Altantzis, S. Bals, G. van Tendeloo and M. Casas-Cabanas, Enhanced electrochemical performance of Li-rich cathode materials through microstructural control, *Phys. Chem. Chem. Phys.*, 2018, **20**(35), 23112–23122.

14 A. S. Menon, S. Ulusoy, D. O. Ojwang, L. Riekehr, C. Didier, V. K. Peterson, G. Salazar-Alvarez, P. Svedlindh, K. Edström, C. P. Gomez and W. R. Brant, Synthetic Pathway Determines the Nonequilibrium Crystallography of Li- and Mn-Rich Layered Oxide Cathode Materials, *ACS Appl. Energy Mater.*, 2021, **4**(2), 1924–1935.

15 D. Y. W. Yu, K. Yanagida, Y. Kato and H. Nakamura, Electrochemical Activities in Li_2MnO_3, *J. Electrochem. Soc.*, 2009, **156**(6), A417.

16 E. McCalla, A. W. Rowe, R. Shunmugasundaram and J. R. Dahn, Structural Study of the Li–Mn–Ni Oxide Pseudoternary System of Interest for Positive Electrodes of Li-Ion Batteries, *Chem. Mater.*, 2013, **25**(6), 989–999.

17 C. R. Brown, E. McCalla, C. Watson and J. R. Dahn, Combinatorial Study of the Li-Ni-Mn-Co Oxide Pseudoquaternary System for Use in Li-Ion Battery Materials Research, *ACS Comb. Sci.*, 2015, **17**(6), 381–391.

18 J. Cabana, S.-H. Kang, C. S. Johnson, M. M. Thackeray and C. P. Grey, Structural and Electrochemical Characterization of Composite Layered-Spinel Electrodes Containing Ni and Mn for Li-Ion Batteries, *J. Electrochem. Soc.*, 2009, **156**(9), A730.

19 E. McCalla, A. W. Rowe, C. R. Brown, L. R. P. Hacquebard and J. R. Dahn, How Phase Transformations during Cooling Affect Li-Mn-Ni-O Positive Electrodes in Lithium Ion Batteries, *J. Electrochem. Soc.*, 2013, **160**(8), A1134–A1138.

20 J. Bareno, C. H. Lei, J. G. Wen, S. H. Kang, I. Petrov and D. P. Abraham, Local structure of layered oxide electrode materials for lithium-ion batteries, *Adv. Mater.*, 2010, **22**(10), 1122–1127.

21 M. J. O'Malley, H. Verweij and P. M. Woodward, Structure and properties of ordered Li_2IrO_3 and Li_2PtO_3, *J. Solid State Chem.*, 2008, **181**(8), 1803–1809.

22 P. S. D. Whitfield, I. J. Davidson, P. W. Stephens, L. M. D. Cranswick and I. P. Swainson, Diffraction analysis of the lithium battery cathode material $Li_{1.2}Mn_{0.4}Ni_{0.3}Co_{0.1}O_2$, *Z. Kristallogr. Suppl.*, 2007, **2**(26), 483–488.

23 D. Mohanty, A. Huq, E. A. Payzant, A. S. Sefat, J. Li, D. P. Abraham, D. L. Wood and C. Daniel, Neutron Diffraction and Magnetic Susceptibility Studies on a High-Voltage $Li_{1.2}Mn_{0.55}Ni_{0.15}Co_{0.10}O_2$ Lithium Ion Battery

Cathode: Insight into the Crystal Structure, *Chem. Mater.*, 2013, **25**(20), 4064–4070.

24 C.-C. Wang, K. A. Jarvis, P. J. Ferreira and A. Manthiram, Effect of Synthesis Conditions on the First Charge and Reversible Capacities of Lithium-Rich Layered Oxide Cathodes, *Chem. Mater.*, 2013, **25**(15), 3267–3275.

25 L. Riekehr, J. Liu, B. Schwarz, F. Sigel, I. Kerkamm, Y. Xia and H. Ehrenberg, Effect of pristine nanostructure on first cycle electrochemical characteristics of lithium-rich lithium–nickel–cobalt–manganese-oxide cathode ceramics for lithium ion batteries, *J. Power Sources*, 2016, **306**, 135–147.

26 J. Zheng, M. Gu, A. Genc, J. Xiao, P. Xu, X. Chen, Z. Zhu, W. Zhao, L. Pullan, C. Wang and J. G. Zhang, Mitigating voltage fade in cathode materials by improving the atomic level uniformity of elemental distribution, *Nano Lett.*, 2014, **14**(5), 2628–2635.

27 R. A. House, H. Y. Playford, R. I. Smith, J. Holter, I. Griffiths, K. J. Zhou and P. G. Bruce, Detection of trapped molecular O_2 in a charged Li-rich cathode by Neutron PDF, *Energy Environ. Sci.*, 2022, **15**(1), 376–383.

28 C. N. R. Rao, Chemical Synthesis of Solid Inorganic Materials, *Mater. Sci. Eng., B*, 1993, **18**(1), 1–21.

29 T. N. L. Doan, K. Yoo, T. K. A. Hoang and P. Chen, Recent Developments in Synthesis of xLi2MnO3(1-x)LiMO2 (M = Ni, Co, Mn) Cathode Powders for High-Energy Lithium Rechargeable Batteries, *Front. Energy Res.*, 2014, **2**, 36.

30 M. P. Pechini, *U.S. Patent No. 3,330,697*, U.S. Patent and Trademark Office, Washington, DC, 1967.

31 B. E. Warren, X-Ray, Diffraction in Random Layer Lattices, *Phys. Rev.*, 1941, **59**(9), 693–698.

32 M. Casas-Cabanas, J. Rodríguez-Carvajal, J. Canales-Vázquez, Y. Laligant, P. Lacorre and M. R. Palacín, Microstructural characterisation of battery materials using powder diffraction data: DIFFaX, FAULTS and SH-FullProf approaches, *J. Power Sources*, 2007, **174**(2), 414–420.

33 G. S. Pawley, Unit-Cell Refinement from Powder Diffraction Scans, *J. Appl. Crystallogr.*, 1981, **14**(6), 357–361.

34 A. A. Coelho, TOPASandTOPAS-Academic: an optimization program integrating computer algebra and crystallographic objects written in C++, *J. Appl. Crystallogr.*, 2018, **51**(1), 210–218.

35 M. Casas-Cabanas, M. Reynaud, J. Rikarte, P. Horbach and J. Rodriguez-Carvajal, FAULTS: A program for refinement of structures with extended defects, *J. Appl. Crystallogr.*, 2016, **49**(6), 2259–2269.

36 J. M. Zheng, X. B. Wu and Y. Yang, A comparison of preparation method on the electrochemical performance of cathode material $Li[Li_{0.2}Mn_{0.54}Ni_{0.13}Co_{0.13}]O_2$ for lithium ion battery, *Electrochim. Acta*, 2011, **56**(8), 3071–3078.

37 R. Shunmugasundaram, R. S. Arumugam and J. R. Dahn, A study of stacking faults and superlattice ordering in some Li-rich layered transition metal oxide positive electrode materials, *J. Electrochem. Soc.*, 2016, **163**(7), A1394.

38 T. Ohzuku and Y. Makimura, Layered Lithium Insertion Material of $LiNi_{1/2}Mn_{1/2}O2$: A Possible Alternative to LiCoO2 for Advanced Lithium-Ion Batteries, *Chem. Lett.*, 2001, **30**(8), 744–745.

